HIGH STRAIN GRADIENT MEASUREMENTS USING MESHLESS METHODS AND COMPUTER VISION

Giancarlo Gómez Gonzáles, giancarlo.g.gonzales@hotmail.com
Marco Antonio Meggiolaro, meggi@puc-rio.br

Pontifical Catholic University of Rio de Janeiro, Department of Mechanical Engineering
Rua Marquês de São Vicente 225, Gávea. Rio de Janeiro, RJ – 22543-900

Abstract. In the present paper, a combined experimental–numerical technique for the measurement of the strain distribution around notches is described using a novel digital image correlation technique. The experimental part of this technique is based on the capture of images at different stages of material deformation when it is subjected to mechanical forces. The Scale Invariant Features Transform (SIFT) is a computer vision algorithm used here to extract distinctive points or features in the collected images. For this purpose, a random texture was painted on the material surface. Then, the displacements are experimentally obtained by tracking the positions of successfully matched SIFT points in an undeformed-deformed pair of images. The points provided by SIFT are selected as nodes in a meshless formulation to generate a numerical approximation for the displacement field and its derivatives. For that, the moving least square method is applied. Thus, the corresponding strain field close to the notch is calculated. To validate the proposed methodology, notched specimens were employed to study the deformation behavior in the regions of stress concentration. The testing results show good agreement and accuracy when compared with the numerical solutions by finite element method.

Keywords: SIFT, meshless methods, high strain gradient, moving least squares.

1. INTRODUCTION

According to Saint-Venant's principle, the strength of material equations are only valid in regions of the material surface sufficiently far enough from sudden changes in geometry and points of load application. These equations are used to calculate the called nominal stresses, in which the effects of geometric discontinuities are not considered. We should be able to evaluate the stress distribution in the neighborhood of the discontinuity and use correctly this information due to most engineering components contain geometric details such as holes, shoulders, keyways, and grooves (generally termed notches). However, under load conditions, the changes in geometry cause local stress peaks that may be several times larger than the nominal stresses calculated for this section. Such discontinuities are called stress raisers, and the regions in which they occur are called areas of stress concentration (Budynas *et al.*, 2011).
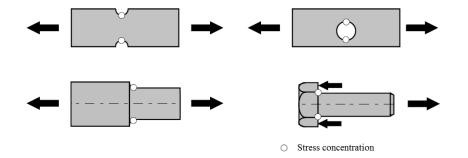

Figure 1. Examples of regions of stress concentrations caused by geometric features.

The areas with high stress concentration lead to a strength degradation and possible premature failure mainly due to fatigue cracking and plastic deformation frequently occurring at these points. The study of stress concentration of notched components under different loading conditions becomes significant and indispensable for a safe design of the component. Therefore, many researchers use experimental methods or analytical/numerical methods for stress/strain analysis.

The strain gage is the most commonly used strain measurement sensors because of simplicity and relatively inexpensive to use. However, its finite size is a limitation for high strain gradients measurement. Moreover, strain gages can only provide local information, which cannot be used to obtain full-field information.

In recent years, optical methods have shown to be a powerful tool in the domain of experimental mechanics. Classical procedures have been significantly improved by recent advances in optical measurement methods and image processing. These full-field measurement techniques lead to high resolution displacement and strain maps which allows more accurate results for mechanical behavior analysis. The main advantage of these techniques is that the measurement does not interfere with the experimental process since there is no contact with the studied specimen.

The Digital Image Correlation is probably one of the most widely used methods due to its simplicity and versatility. Many applications of this technique can be found in the literature for the determination of full-field strain fields, including those around notches (Sutton *et al.* 2009; Qian *et al.* 2011, Góes *et al.* 2011). The DIC uses tracking and image registration techniques to determine regions correspondences between two images of a specimen in different stages of mechanical deformation. Consecutively, physical quantities related to the element such as displacement and deformation are easily obtained. This method can be used with a single camera system to measure in-plane displacement/strain fields on planar objects. For more complex geometries, the use of two cameras allows the measurement of 3-D displacement/strain fields. Commonly, the correspondences subsets in area-based techniques are defined by the normalized cross correlation (NCC), sum of squared differences (SSD) or variants of these methods. In order to perform this process, a pattern with random characteristics on the specimen surface is required.

In computer vision, another approach for solving the correspondence problem is the use of local descriptors constructed from simples features extracted from images. Among these approaches, the Scale Invariant Feature Transform (SIFT) proposed by Lowe (Lowe, 1999 and Lowe, 2004) has become popular feature extractor. It has been successfully used in several vision-based applications (Lee and Song, 2010, Castle and Murray, 2011), because of its good performance and robustness (Mikolajczyk and Schmid, 2005).

This study proposes a novel method for full-field strain measurements incorporating the SIFT technique in the image correlation process. The SIFT algorithm automatically detects homologous features, called keypoints, in the sequence of images recorded during mechanical testing. The nodal displacements are measured by tracking the positions of successfully matched keypoints in an undeformed-deformed pair of images. Then, the meshless approximation is used to define the continuous displacement field and therefore, the corresponding strain field can be estimated. These numerical methods are mainly characterized by not requiring a mesh to represent the problem domain, depending exclusively on a set of nodes scattered within it (Liu, 2005 and Liu and Gu., 2009). This flexibility permits that the SIFT keypoints are selected as nodes in a meshless formulation. Thus, the problems associated with mesh generation are eliminated.

The meshless methods have been considerably improved (Liu, 2009) and successfully applied for deformations and strain measurement using optical methods (Andrianopoulos, 2006). In this study, a formulation similar to the one proposed by Belytschko *et al.* (1994) is adopted, the element free Galerkin method, which uses the Moving Least Squares procedure for the interpolation of the displacement function.

To validate the proposed methodology, the deformation behavior in the region of stress concentration of a notched specimen was investigated. The results obtained by this method were compared with the results obtained from the numerical analysis by using a commercial finite element method (FEM) software.

2. THE SCALE INVARIANT FEATURE TRANSFORM TECHNIQUE

Scale-invariant feature transform (SIFT) is an algorithm in computer vision to detect and describe features in images. The SIFT features are local and based on the appearance of the object at particular interest points. The descriptor associates a vector of information to each single detected point, which identifies their appearance compactly and robustly. The SIFT descriptors are invariant to image scale and rotation. They are also robust to changes in illumination, noise and minor changes in viewpoint. In addition to these properties, the features are highly distinctive, in the sense that a single feature can be correctly matched with high probability against a large database of features from many images.

2.1. SIFT Algorithm Steps

Scale-space Extrema Detection: In the first stage, a Difference-of Gaussian function is applied to identify potential interest points. This stage of computation searches over all scales and image locations.

Keypoint Localization and Filtering: At each candidate location, a detailed model is fit to determine location and scale. Unstable keypoints are rejected because they are sensitive to noise.

Orientation Assignment: One or more orientations are assigned to each keypoint location based on local image gradient directions. All future operations are performed on image data that has been transformed relative to the assigned orientation, scale, and location for each feature, therefore providing invariance to these transformations.

Keypoint Descriptor: The local image gradients are measured at the selected scale in a neighborhood around the keypoint. The neighborhood is divided into $4 \times 4 = 16$ sub-regions and 8-bin histogram of weighted gradients is computed for each sub-region, see Fig. 2. The 16 histograms are then concatenated into a 128-dimensional vector. In addition, the descriptor is normalized to enhance invariance to changes in illumination.
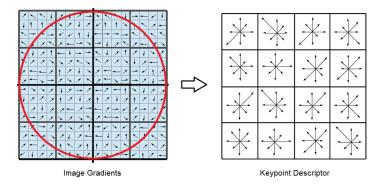
Image Gradients   Keypoint Descriptor

Figure 2. SIFT descriptor containing 128 elements computed from a set of 16 histograms in a 4x4 grid.

2.2. Matching

For image matching, the extracted SIFT features and their descriptors are stored in a database. The best match for each descriptor is found by identifying the nearest neighbor (closest descriptor) in the database of keypoints descriptors from the processed images. In order to discard poorly matched keypoints, a subsequent threshold is used which rejects matches that are too ambiguous. If the distance ratio between the closest neighbor and the second-closest neighbor is below some threshold, then the match is kept, otherwise the match is rejected and the keypoint is removed.
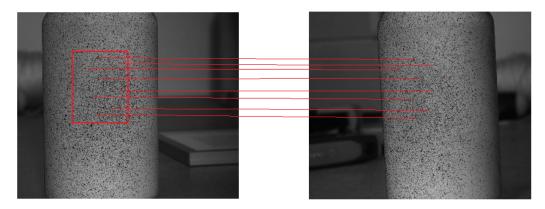

Figure 3. Example of matching process. SIFT keypoints were matched in this pair images of the same object from different viewpoints. For visibility, only some of these matches are shown.

3. MESHLESS FORMULATION

Meshless methods use a set of nodes scattered within the problem domain and its boundaries. These sets of scattered nodes are called field nodes, and they do not form a mesh, meaning it does not require any a priori information on the relationship between the nodes for the interpolation or approximation of the unknown functions of field variables (Liu, 2009).

Since there is no mesh of elements in an meshless method, the *u*-component of the displacement field at any point $x^T = [x, y, z]$ within the problem domain is interpolated using the displacements at a number of nodes around it. These nodes constitute the local support domain of the point at x. Mathematically,

$$u(\mathbf{x}) = \sum_{i}^{n} \phi_i(\mathbf{x}) u_i = \mathbf{\Phi}(\mathbf{x})\mathbf{U} \tag{1}$$

In this equation, n is the number of nodes in the support domain of x, u_i the displacement of the *i-th* node in the support domain, U the vector containing all the nodal displacement variables, $\phi_i(x)$ is the shape function of the *i-th* node determined using these nodes included in the support domain of x and $\Phi(x)$ the matrix that collects all the shape function values:

$$\mathbf{\Phi}(\mathbf{x}) = \begin{bmatrix} \phi_1(\mathbf{x}) & \phi_2(\mathbf{x}) & ... & \phi_n(\mathbf{x}) \end{bmatrix} \tag{2}$$

As the shape functions will not be used regarded as zero outside the local support domain in an meshless method, we often say that the shape functions is locally support. A local support domain of a point x determines the number of nodes to be used to support or approximate the function value at x. Accordingly with Liu (2009), the use of an influence domain is an alternative way to select node for interpolation in domains with highly non-regularly distributed nodes.

The influence domain is defined as a region where a node exerts its influences, and it can be different from node to node, as shown in the Fig. 4. The nodes *i* and *k* are within the support domain of point x. Later these nodes will be used to construct the shape function for the point x. Note that the node *j* does not have any influence on point x, consequently, the node *j* will be not used.
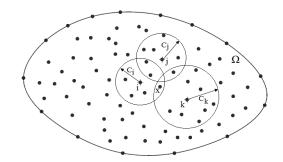

Figure 4. Example of Influence Domains with a circular shape for the nodes i, j and k with radius of C_i, C_j and C_k, respectively. Note that the influence domain is usually centered in the point of interest.

For a point of interest at x, the dimension of the influence domain, dm_i, is determined by

$$dm_i = \alpha_s \cdot C_i \tag{3}$$

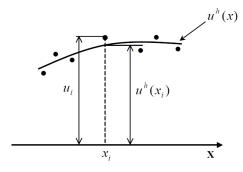where α_s is a multiplier support that controls the actual dimension of the domain.

Accordingly with Liu and Gu (2005), when the influence domain is too small ($\alpha_s < 2.0$), there are not enough nodes used to perform the function approximation for the field variables. In addition, when the influence domain is too large ($\alpha_s > 4.0$), the constructed shape functions become too smooth to represent the local properties of the field variables. Hence, a proper influence domain should be used to ensure a reliable solution.
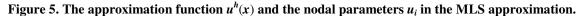
3.1. MLS Approximation

The MLS strategy is based on the construction of shape functions to generate the approximation of *u(x)*, denoted here as $u^h(x)$, influenced by the values at the nodes positioned in the support domain of the point of interest, x. The local approximation is defined by (Belytschko *et al.* 1994)

$$u^h(\mathbf{x}) = \sum_{j}^{m} p_j(\mathbf{x})a_j(\mathbf{x}) = \mathbf{P}^T(\mathbf{x})\mathbf{a}(\mathbf{x}) \tag{4}$$

where $\mathbf{P}^T(x)$ is a linear polynomial basis of order *m* and $a(x)$ is a vector of coefficients to be determined.

Figure 5. The approximation function $u^h(x)$ and the nodal parameters u_i in the MLS approximation.

In Tab. 1 we present some basis functions in a two-dimensional domain.

Table 1. Polynomial basis in 2D

Constant (*m* = 1)	$[1]$
Linear (*m* = 3)	$[1 \quad x \quad y]$
Quadratic (*m* = 6)	$[1 \quad x \quad y \quad x^2 \quad y^2 \quad xy]$

The unknown coefficients $a(x)$ are obtained by minimizing the difference between the local approximation and the function, through

$$J = \sum_i^n w(\mathbf{x} - \mathbf{x_i})\left[\mathbf{P}^\mathrm{T}(\mathbf{x}_i)\mathbf{a}(\mathbf{x}) - u_i \right]^2 \tag{5}$$

where $w(x - x_i)$ is known as the weight function and n is the number of points in the neighborhood of x for which the weight function $w(x - x_i) \neq 0$.

The functional J can be minimized by setting the derivative of J with respect to $a(x)$ equal to zero. It results in the following linear relation between $a(x)$ and U:

$$\mathbf{A}(\mathbf{x}) \cdot \mathbf{a}(\mathbf{x}) = \mathbf{B}(\mathbf{x}) \cdot \mathbf{U} \tag{6}$$

where the matrices A and B are defined by

$$\mathbf{A}(\mathbf{x}) = \sum_i^n w(\mathbf{x} - \mathbf{x}_i)\mathbf{P}(\mathbf{x}_i)\mathbf{P}^\mathrm{T}(\mathbf{x}_i) \tag{7}$$

$$\mathbf{B}(\mathbf{x}) = w(\mathbf{x} - \mathbf{x}_i)\mathbf{P}^\mathrm{T}(\mathbf{x}_i) \tag{8}$$

The nodal displacement of the field variables are represented by the vector U:

$$\mathbf{U} = \sum_i^n u_i \tag{9}$$

The solution of the linear system (Equation 6) is:

$$\mathbf{a}(\mathbf{x}) = \mathbf{A}^{-1}(\mathbf{x}) \cdot \mathbf{B}(\mathbf{x}) \cdot \mathbf{U} \tag{10}$$

Substituting Eq. (10) into Eq. (4), the MLS approximation is obtained

$$u^h(\mathbf{x}) = \sum_i^n \sum_j^m p_j(\mathbf{x})\left(\mathbf{A}^{-1}(\mathbf{x})\mathbf{B}(\mathbf{x}) \right)_{ji} u_i \tag{11}$$

where comparing with Eq. (1), the shape function ϕ_i associated with the node x_i is defined by

$$\phi_i(\mathbf{x}) = \sum_j^m p_j(\mathbf{x})\left(\mathbf{A}^{-1}(\mathbf{x})\mathbf{B}(\mathbf{x}) \right)_{ji} \tag{12}$$

This can be written shortly as

$$\phi_i = \mathbf{P}^\mathrm{T}\mathbf{A}^{-1}\mathbf{B}_i \tag{13}$$

Then, the partial derivatives of the shape function can be obtained from (Belytschko *et al.* 1994)

$$\phi_{i,x} = \mathbf{P}^\mathrm{T}_{,x}\mathbf{A}^{-1}\mathbf{B}_i + \mathbf{P}^\mathrm{T}\left(\mathbf{A}^{-1} \right)_{,x}\mathbf{B}_i + \mathbf{P}^\mathrm{T}\mathbf{A}^{-1}\mathbf{B}_{i,x} \tag{14}$$

$$\phi_{i,y} = \mathbf{P}^\mathrm{T}_{,y}\mathbf{A}^{-1}\mathbf{B}_i + \mathbf{P}^\mathrm{T}\left(\mathbf{A}^{-1} \right)_{,y}\mathbf{B}_i + \mathbf{P}^\mathrm{T}\mathbf{A}^{-1}\mathbf{B}_{i,y} \tag{15}$$

where the subscript represents the spatial derivation in cartesian coordinates frame.

Referring to the Eq. (14) and Eq. (15), the spatial derivative of the weight function is necessary to compute the spatial derivative of the A and B matrices. This derivative is computed easily using the chain rule of differentiation as,

$$dw_{i,x} = dw_{i,r} \cdot dr_{,x} \tag{16}$$

$$dw_{i,y} = dw_{i,r} \cdot dr_{,y} \tag{17}$$

Nevertheless, Eq. (1) can also be used for the displacement component $v(\boldsymbol{x})$, i.e.

$$v^h(\mathbf{x}) = \sum_i^n \phi_i(\mathbf{x}) v_i \tag{18}$$

Thus, the displacement field in the deformed surface is defined as

$$\begin{Bmatrix} u \\ v \end{Bmatrix}^h = \sum_i^n \begin{bmatrix} \phi_i & 0 \\ 0 & \phi_i \end{bmatrix} \begin{Bmatrix} u_i \\ v_i \end{Bmatrix} \tag{19}$$

Using Eq. (13) and solving for x and y, the strain field is obtained by:

$$\begin{Bmatrix} \varepsilon_x \\ \varepsilon_y \\ \varepsilon_{xy} \end{Bmatrix}^h = \sum_i^n \begin{bmatrix} \dfrac{\delta}{\delta x} & 0 \\ 0 & \dfrac{\delta}{\delta y} \\ \dfrac{\delta}{\delta y} & \dfrac{\delta}{\delta x} \end{bmatrix} \begin{bmatrix} \phi_i & 0 \\ 0 & \phi_i \end{bmatrix} \begin{Bmatrix} u_i \\ v_i \end{Bmatrix} = \sum_i^n \begin{bmatrix} \phi_{i,x} & 0 \\ 0 & \phi_{i,y} \\ \phi_{i,x} & \phi_{i,y} \end{bmatrix} \begin{Bmatrix} u_i \\ v_i \end{Bmatrix} \tag{20}$$

4. EXPERIMENTAL SETUP
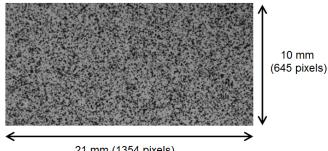
4.1. Image Acquisition System

The image acquisition process is based on two synchronized CCD cameras observing the material surface during the experiment from different directions. The 5.0 Megapixel CCD cameras (Point Grey GRAS-50S5M) fitted with Tamron A031 lenses (AF28-200mm F/3.8-5.6) were mounted on a tripod positioned in front of the specimen. This results in a field of view of about 38×25 mm^2 with a pixel resolution of. 15.5 µm in the object plane. A fiber optic illuminator was used to illuminate the area of interest.

In this case, the system is located on a fixed position, i.e. the calibration parameters are not changed during the performed mechanical test. A camera calibration process is performed to determine the intrinsic and extrinsic parameters for camera systems. Thereafter, these information are used to recover 3D position from the 2D images captured by the cameras. The quality of the camera calibration is an important factor that determines the accuracy of the inspection system.

4.2. Preparation of specimen surface

Concerning the specimen preparation, this procedure aims to provide a large number of possible points of interest that can be detected by the SIFT algorithm. Accordingly, the sample surface is covered with a uniform white paint and thereafter black dots are inserted by spray painting, see Fig. 6.

The number of detected SIFT points inside the region of interest is particularly important, in order to obtain a reliable and accurate measurements. The sprayed dots must cover densely the analyzed area, homogeneous patterns must be avoided.

10 mm
(645 pixels)

21 mm (1354 pixels)

Figure 6. Surface detail of the specimen covered with painted speckles.

4.3. Procedure

For experimental validation, a cantilevered beam-like specimen is subjected to a concentrated load P applied at the free end, see Fig. 7. The rectangular beam has a semi-circular notch of radius 5 mm at the middle of the length. The mechanical properties of the specimen are shown in Tab. 2.

The image captured with the specimen in the unloaded stage is selected as the reference image. All the results have to be calculated with respect to this image, typically acquired in the beginning of the experiment. The deformed image is captured when a load of 4.7N is applied.

Table 2. Mechanical properties and dimensions of specimen.

Material	Polycarbonate
Young's modulus (E) [*]	2.2 GPa
Poisson's ratio (v) [*]	0.38

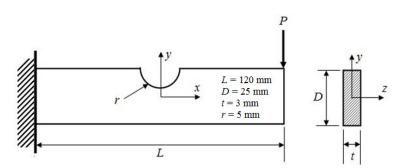[*] experimentally measured in laboratory.

Figure 7. Sketch of the experimental set-up.

5. ANALYSIS AND RESULTS

All method described here has been implemented in a software program using Matlab® (Mathworks, 2013) to evaluate displacement (Equation 19) and strain fields (Equation 20), respectively, for a given pair of undeformed-deformed images.

First of all, an area of interest is manually defined by the user. As shown in Fig. 8, the red rectangle indicates the selected area of interest for this analysis. Then, the SIFT algorithm automatically detects a number of characteristic points between the reference image and the deformed image. The matching process provides the locations in the two images for the same keypoints, i.e. for a specific point in the reference image, a unique point in the deformed image has identified as its corresponding one.

Thereafter, the spatial coordinates of these points are calculated. For this purpose, the matching process between each stereo-pair images provides the locations in the two views for the same point. Once both intrinsic and extrinsic parameters of the stereo vision system are known, the reconstruction problem can be solved unambiguously by stereo triangulation. The set of successfully matched keypoints and their locations in the captured images are shown in Fig. 8. As no elements are used in meshless methods, domain representation is performed by means of this nodal distribution.
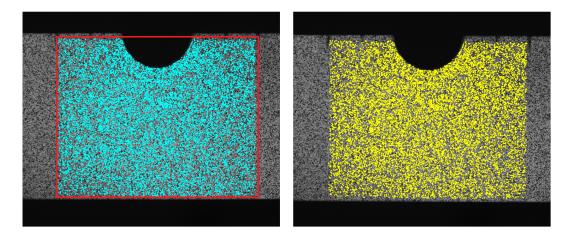

Figure 8. The figure shows 10533 keypoints successfully matched by SIFT algorithm in this pair of undeformed-deformed images. (Right) Reference Image. (Left) Deformed Image.

After the images processed by SIFT, the meshless method above-described is applied. In the present study, a quadratic basis function of six terms was used (see Tab.1). The weight function introduced in the Eq. (5) plays an important role in the performance of the method. The choice of this function is more or less arbitrary as long as the function to be positive and continuous. However, there are many weight functions that can meet these conditions.

In this paper, we will use the Exponential weight function with a circular domain of influence (Belytschko et. al. 1995):

$$w_i = \begin{cases} e^{-(r/a)^2} & , & |r| \leq 1 \\ 0 & , & |r| > 1 \end{cases} \tag{21}$$

where r is the influence radius of the node i and a is a constant (usually $a = 0.3$).

The dimension of r is calculated is calculated by the equation:

$$r = \frac{\|\mathbf{x} - \mathbf{x}_i\|}{dm_i} \tag{22}$$

The derivatives of the Gaussian weight function are calculated using Eq. (16) and Eq. (17), we have

$$w_{i,x} = w_{i,r} \frac{x - x_i}{r\, dm_i^2} \tag{23}$$

$$w_{i,y} = w_{i,r} \frac{y - y_i}{r\, dm_i^2} \tag{24}$$

with

$$w_{i,r} = \begin{cases} \frac{-2r}{a^2} e^{-(r/a)^2} & , & |r| \leq 1 \\ 0 & , & |r| > 1 \end{cases} \tag{25}$$

With these parameters, the meshless approximations are obtained for each supported node based on the multiplier support, the scaling parameter α_s defined in the Eq. (3), associated with it. Commonly, the dimensionless size of α_s should be predetermined by the analyst. According to computed experience, a $\alpha_s = 2.0$ to 4.0 lead to good results.

In this study, we established the size of the domain to be variable. The aim of this variability is to get more accurate results by decreasing the supporting nodes for interpolation in areas with high stress concentration in which higher accuracy is commonly required. In opposite, the numbers of nodes are increasing in areas when the stress distribution to be uniform. For this purpose, a methodology was established to determine the values of α_s for each supported node. Firstly, a minimum number of supporting points has to be defined. We fixed the minimum influence domain at 400 neighbors points, circle domain with radius of approximately 2.5mm, which are selected using a nearest neighbor algorithm based on Euclidean distance, see Fig. 9.
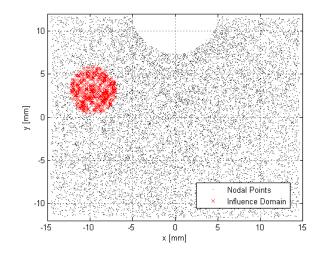

Figure 9. Nodal distribution provided by SIFT algorithm. The circular neighborhood represents the influence domain for specific supported node.

Then, a first meshless approximation is computed with fixed value of α_s, rather than high values (3.5 or 4.0). The magnitude of the gradient of this resultant approximation in the direction of the notch will show how fast the strain rises in that direction, see Fig. 10.
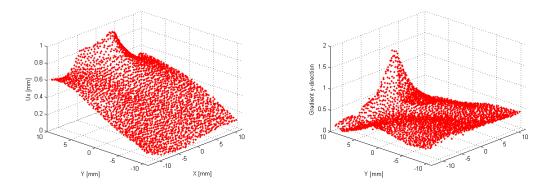
Figure 10. (Right) First meshless approximation with fixed value of α_s for the strain component in the x-direction. (Left) Normalized gradient function in the direction of the notch.

This information is useful for choosing a suitable value of α_s at each evaluation point, using for this purpose the test function shown in the Fig. 11. This function was performed with numerical simulations to problems of which the solutions were known beforehand.
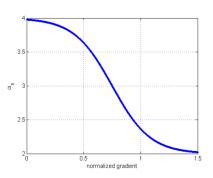

Figure 11. Test function for calculate the values of α_s parameter.

Thereafter, the approximations are re-computed with the new values of α_s and, finally, the strain distribution of the notched sample is visualized as shown in the Fig. 12. The strain intensification in the notch ground is clear indicated.
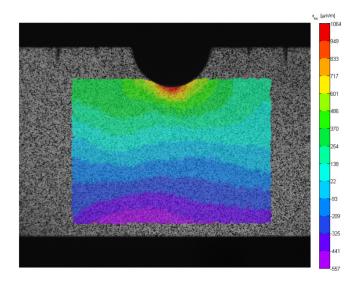

Figure 12. SIFT-Meshless full-field strain plots at 4.7N.

To demonstrate the capability of full field measurement, the finite element analysis using commercial package code ANSYS is performed to determine the strain distribution near the stress concentration area. Boundary conditions and the loading conditions are applied for simulate the same conditions with the experiment. Then, the experimental results are compared with the FEM analysis shown in the Fig. 13. Good agreement between them is observed, which validates the correctness of the present method.
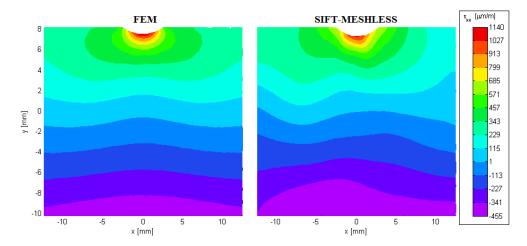
Figure 13. Comparison of SIFT-Meshless and FEM results.

For the notched specimen there is a variation of the transverse strain across the width of the specimen. The Fig. 14 shows the axial-strain distribution at $x = 0$ of the experimental method against the expected numerical solution. The results show that two strain distribution curves have the same trend, which indicates that the proposed methodology gives reliable solutions for high gradient strain measurement.
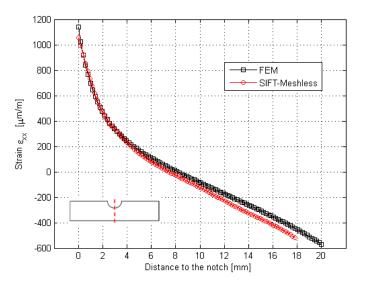

Figure 14. Comparison of strains variations along the notch for a semicircular concentrator.

The information concerning the differences between the results obtained in the Fig. 14 is listed in the Tab. 3 shown below.

Table 3. Differences between SIFT-Meshless measurements and numerical analyses by FE

Average Deviation (µε)	47
Root Mean Square (µε)	51
Maximum Deviation (µε)	78

6. CONCLUSIONS

The present paper provides an alternative path for the measurement of strain distribution in areas of stress concentration based on computer vision and meshless methods. The SIFT technique is introduced to obtain the displacement information of a specimen surface in a given pair of undeformed–deformed images. The use of SIFT descriptors gives robustness and full automaticity to this process. Thereafter, a meshless formulation with variable influence domain is proposed here to generate numerical approximations for the displacement field and its derivatives. By using this procedure, the solution is performed without loss of information and with high accuracy, mainly in the region near of the notch in which high strain gradient are expected. Nevertheless, the use of stereo vision system allows that this methodology can be easily expanded for three-dimensional measurements.

The full-field strain distribution of a rectangular beam with a semicircular notch is measured to validate the proposed methodology. The resulting strain field in the region around the notch is compared with the finite element predictions. The experimental results agree well, demonstrating that the proposed method can be a useful tool for the characterization of behavior in the regions of stress concentration. In this way, high strain gradients due to notches can be quantitatively detected.

For future works, the authors plan to apply the proposed method to map the strain fields around sharp notches and crack tips.

7. REFERENCES

Andrianopoulos, N.P., 2006, "Full-Field Displacement Measurement of a Speckle Grid by using a Mesh-Free Deformation Function", Strain, Vol. 42, No. 4, pp. 265–271.

Belytschko, T., Lu, Y.Y. and Gu L., 1994, "Element free Galerkin methods". International Journal for Numerical Methods in Engineering. Vol. 37, pp. 229–256.

Belytschko, T., Organ, D. e Krongauz, Y., 1995, "A coupled finite element-element-free Galerkin method". Comput. Mech. Vol. 17, pp. 186–195.

Budynas, R.G. and Nesbitt, J.K., 2011, "Shigley's Mechanical Engineering Design", 9th edition, McGraw-Hill, New York.

Castle, R.O. and Murray, D.W., 2011, "Keyframe-based recognition and localization during video-rate parallel tracking and mapping", Image Vision Comput., pp. 524-532.

Góes, R.C.O., Rodrigues, L.D.R., Castro Neto, J., Castro, J.T.P., Freire, J.L.F. and Martha, L.F., 2011, "Measurement of elastic-plastic strains around notches using DIC techniques", Proceedings of the 21st Brazilian Congress of Mechanical Engineering, Natal, Brazil.

Liu, G.R. and Gu, Y.T., 2005, "An Introduction to Meshfree Methods and their Programming", Springer, The Netherlands.

Liu, G.R., 2009, "Meshfree methods: Moving Beyond the Finite Element Method", 2nd Edition, CRC Press, Boca Raton, USA.

Lee, Y.J., Song, J.B., 2010, "Autonomous salient feature detection through salient cues in an HSV color space for visual indoor simultaneous localization and mapping", Advanced Robotics, Vol. 24, No.11, pp. 1595-1613.

Lowe, D.G., 1999. "Object recognition from local scale-invariant features", International Conference on Computer Vision", Corfu, Greece, Vol. 2, pp. 1150–1157.

Lowe, D.G., 2004. "Distinctive image features from scale invariant key points", International Journal of Computer Vision, Vol. 60, No. 2, pp. 91–110.

Matlab, 2013, "User Manual", Mathworks.

Mikolajczyk, K. and Schmid, C., 2005, "A performance evaluation of local descriptors. IEEE Transactions on Pattern Analysis & Machine Intelligence", Vol. 27, No.10, pp. 1615-1630.

Qian, C., Harper, L.T., Turner, T.A. and Warrior, N.A., 2011, "Notched behaviour of discontinuous carbon fibre composites: comparison with quasi-isotropic non-crimp fabric", Composites Part A: Applied Science and Manufacturing. Vol. 42, No 3, pp. 293-302.

Sutton, M.A., Orteu, J.J. and Schreier, H.W., 2009, "Image Correlation for Shape, Motion and Deformation Measurements: Basic Concepts, Theory and Applications", Springer, New York, USA.

8. RESPONSIBILITY NOTICE

The authors are the only responsible for the printed material included in this paper.